


Cite this: *Energy Adv.*, 2024,  
3, 459

## 2D bifunctional tungsten disulfide-embedded UiO-66 (WS<sub>2</sub>@UiO-66) as a highly active electrocatalyst for water splitting

Muhabbat Shah, Uzair Abdullah, Erum Pervaiz \* and Maryum Ali

Effective water-splitting electrocatalysts provide great potential for the production of hydrogen as fuel in renewable and sustainable energy devices. Electrocatalysts become the bottleneck in the process of achieving easy and cost-effective water-splitting and require tremendous attention on the catalyst design. An economical, greatly stable, and effective electrocatalyst with low activation potential is usually required. In this study, we present a solvothermal method for the synthesis of a highly effective electrocatalyst, denoted as WS<sub>2</sub>@UiO-66, to facilitate rapid and efficient water splitting. WS<sub>2</sub>@UiO-66 forms a heterostructure, allowing for efficient overall water splitting. Open structures with many active sites are accessible to the reactants in this bifunctional design, which promotes mass diffusion and electron transport. In an alkaline solution, WS<sub>2</sub>/UiO-66 exhibits exceptional HER and OER activity, requiring an HER overpotential of 121 mV and OER overpotential of 220 mV to yield a current density of 10 mA cm<sup>-2</sup>. The best catalyst shows a smaller Tafel value of 272 mV dec<sup>-1</sup> and 140 mV dec<sup>-1</sup> for HER and OER, respectively. Furthermore, at a current density of 10 mA cm<sup>-2</sup>, WS<sub>2</sub>@UiO-66 can sustain HER/OER without a substantial loss for 24 hours. The outstanding bifunctional catalytic performance of WS<sub>2</sub>@UiO-66 can significantly accelerate its utilization in water splitting. This research may pave the way for the development of new methods for cost-effective energy conversion and storage catalysts.

Received 24th July 2023,  
Accepted 17th December 2023

DOI: 10.1039/d3ya00348e

rsc.li/energy-advances

### 1. Introduction

Because of the rising energy crises and environmental pollution, exploration and advancement in the field of hydrogen energy have become highly urgent.<sup>1–3</sup> Hydrogen is considered a sustainable fuel and a favorable future energy carrier owing to the unlimited source of water and zero greenhouse gas emissions.<sup>4,5</sup> Hydrogen production by electrocatalytic water splitting is one of the most innovative technologies for resolving environmental challenges and finding a sustainable energy source. For its extremely high energy density and caloric values, hydrogen can be broadly employed as a fuel in transportation and stationary power.<sup>6,7</sup> However, many parameters, other than cost, limit its large-scale application. To manage these parameters, designing a suitable catalyst is the way forward. A variety of transition metal sulfides, nitrides, and carbides are being investigated as water-splitting electrocatalysts. These materials are suitable for HER and OER because of their high catalytic activity, exceptional durability, and efficient charge transfer. They are dependable for long-term

applications owing to their stability under challenging electrochemical conditions. Additionally, because of their adjustable electronic and structural characteristics, the performance of the catalyst can be customized. Some metal nitrides and sulfides, such as iron nitride (FeN) and molybdenum disulfide (MoS<sub>2</sub>), have abundant resources, which lowers production costs. Researchers are continually fine-tuning the properties of these materials to improve their performance in a variety of electrochemical environments.<sup>8–10</sup> By decreasing the activation energy of a reaction, we can increase the reaction rate and improve the energy conversion efficiency, which is a crucial aspect of catalyst design.<sup>11</sup> Developing catalytically active bifunctional catalysts with suitable conductivity and charge transfer for an efficient OER and HER is difficult and tedious. For HER and OER, researchers are looking at novel catalyst materials with high energy conversion rates and low overpotentials. Some of these bifunctional heterostructures exhibit the increased performance of OER and HER processes, resulting in the production of hydrogen fuel. Water splitting, powered by variable renewables such as wind power and solar, may create sustainable and high-purity hydrogen at a low cost.<sup>12,13</sup> Although noble metal catalysts are currently the most efficient for water splitting, their scarcity and high cost make them impractical for large-scale applications from an economic standpoint.<sup>14,15</sup>

Heterogeneous Catalysis Lab, Department of Chemical Engineering, School of Chemical and Materials Engineering (SCME), National University of Sciences & Technology (NUST), Sector H-12, Islamabad, 44000, Pakistan.  
E-mail: erum.pervaiz@scme.nust.edu.pk; Tel: +92-5190855103

As an alternative to noble-metal catalysts, transition metal sulfides are being constantly explored for their potential. As they are abundant in nature, the cost of the catalysts will be significantly reduced.<sup>16,17</sup> However, their poor efficiencies for HER and OER fall short of the commercial need for water electrolysis. As a result, the exploitation of highly stable and active earth-abundant catalysts should be given top priority.<sup>14,18,19</sup> Heterostructure electrocatalysts have recently demonstrated advantages in water splitting over single-component catalysts. The heterostructures exhibit abundant exposed edges and surface defects, which arise from lattice distortion and ligand mismatch.<sup>20–22</sup> During the HER or OER processes, these defect centers have the potential to serve as active sites for the adsorption of intermediates. Furthermore, the 3D design enables rapid mass dispersion and greatly lowers the overpotential, notably at high current densities for OER and HER.<sup>23,24</sup> A recent study has shown that 2D materials based on WS<sub>2</sub> might be effective electrocatalysts due to the hydrogen adsorption free energy being close to the thermoneutral zone ( $\Delta G \approx 0$ , i.e., the Gibbs free energy change is approximately zero), of transition metals and chalcogenides.<sup>25–27</sup> Exfoliation of the WS<sub>2</sub> liquid phase nanosheets is widely acknowledged as a reliable method for producing large yields of active layered LPE (liquid phase exfoliated)-WS<sub>2</sub> nanosheets. The electrocatalysts are greatly aided by LPE-WS<sub>2</sub>, which has extensively exposed edges and a low impedance-to-charge transfer.<sup>26</sup> Tungsten disulfide (WS<sub>2</sub>) is another TMD material that has a similar crystal and electrical structure to MoS<sub>2</sub>, and has been the subject of current research due to its high HER activity.<sup>28,29</sup> The HER performance of the WS<sub>2</sub> catalysts is comparable to that of well-known catalysts, such as MoS<sub>2</sub>, CoSe<sub>2</sub>, and CoS<sub>2</sub>. However, WS<sub>2</sub> is a preferable alternative electrocatalyst material due to its abundant reserves, low cost, and higher conductivity. The stability of the material is considered to be a key factor for hydrogen energy production. WS<sub>2</sub> is more stable than other electrocatalysts, and has been shown to have highly efficient electrocatalytic activity for HER. The electrocatalytic activity of WS<sub>2</sub> can be enhanced *via* defect engineering.<sup>30–32</sup> The catalytic efficiency can be considerably increased by changing the structure of WS<sub>2</sub>, a typical two-dimensional material, to expose more active sites.<sup>33</sup>

UiO-66 is a metal–organic framework (MOF) that comprises Zr as the active metal center and benzen-1,4-dicarboxylate (BDC) as the organic linker. It forms octahedral nanoparticles with a substantial surface area. The strong bond between Zr(IV) and the carboxylate O atom leads to high charge density and bond polarization. Remarkably, UiO-66 demonstrates exceptional stability in both organic solvents and water, showcasing outstanding chemical, electrical, and mechanical properties. These advantageous attributes make UiO-66 a highly promising candidate for water-splitting applications.<sup>34,35</sup> Developing composites is one of the many strategies for enhancing electrical conductivity that can be used to overcome the big barrier.<sup>36,37</sup>

Changqi Sun *et al.* discovered that the HER activity can be enhanced by tuning the intrinsic conductivity of WS<sub>2</sub> in N-doped WS<sub>2</sub> nanosheets. Despite substantial progress, the exploration for

HER catalysts is mostly focused on the development of noble metal-free electrocatalysts, overlooking the incorporation of additional driving elements.<sup>27</sup> The strong connection between WS<sub>2</sub> and the positively charged surfactant made 1T'-WS<sub>2</sub> very stable after surface treatment, allowing it to stand effective dissemination in a polar solvent. The 1T'-WS<sub>2</sub> catalyst exhibited a low overpotential of 200 mV, a small Tafel slope of 50.4 mV dec<sup>-1</sup>, and demonstrated exceptional stability at a current density of 10 mA cm<sup>-2</sup>.<sup>38</sup> Additionally, during the alkaline HER process, enhanced cycle stability was discovered, viewing its potential for future applied applications.<sup>39</sup> Tayebi *et al.* studied WS<sub>2</sub>/WO<sub>3</sub>, which was synthesized for the photoelectrochemical water splitting process. The current density of the produced catalyst was extremely high. When the WS<sub>2</sub> nanosheets were deposited, the current density rose dramatically, especially for the WO<sub>3</sub>/WS<sub>2</sub> electrode, with peaks of about 6.6 mA cm<sup>-2</sup> current density at 1.75 V vs. Ag/AgCl.<sup>40</sup> Another study found that the electrocatalyst activity significantly improved when WS<sub>2</sub> nanosheets and CdS were combined (WS<sub>2</sub>/CdS). In the photoelectrochemical overall water splitting, the nanostructures showed a significantly higher photocurrent density than the pristine sulfide of 0.15 mA cm<sup>-2</sup> at 1.23 V vs. RHE.<sup>41</sup> Peng *et al.* studied the 3D Co<sub>9</sub>S<sub>8</sub>/WS<sub>2</sub> electrode material configuration and reported it an effective electrocatalyst for splitting water. In an alkaline medium, electrocatalysts with hydrogen-evolving 3-D electrodes may yield current densities of up to 10 mA cm<sup>-2</sup> with an overpotential of 138 mV. This multifunctional electrode may also be used to build a high-performance alkaline electrolytic cell boasting a cell voltage of 1.65 V at 10 mA cm<sup>-2</sup>.<sup>42</sup>

This paper proposes a rational design of a WS<sub>2</sub>@UiO-66 2D nanostructure for overall alkaline water splitting. These WS<sub>2</sub>@UiO-66 2D nanostructures on nickel foam can minimize WS<sub>2</sub> agglomeration, promote mass diffusivity, advance the electron transport, and provide HER and OER additional active sites. The heterojunction interface between the WS<sub>2</sub> and UiO-66 phases generates a synergistic effect, enabling rapid charge transit, which may dramatically improve the HER and OER activity in alkaline media. The WS<sub>2</sub> film is made up of tiny WS<sub>2</sub> clusters built up of smaller WS<sub>2</sub> nanosheets, and this hierarchical film may be employed as a self-supported electrode for HER when combined with a metal substrate. The WS<sub>2</sub> nanosheets' random orientations and small sizes would considerably aid in exposing active edge locations. As a result, the WS<sub>2</sub> film electrocatalyst exhibits superior electrocatalytic activity, including a low overpotential (121 mV) to reach a current density of 10 mA cm<sup>-2</sup> and excellent catalytic durability by performing ultra-long HER operations in a basic environment at a static overpotential (> 24 h).

## 2. Experimental section

### 2.1 Chemicals

For the fabrication of all of the electrocatalysts, analytical grade chemicals and compounds were utilized (with no processing or purification). Chemicals include sodium tungstate dihydrate



( $\text{Na}_2\text{WO}_4 \cdot 2\text{H}_2\text{O}$ ) (CAS# 10213-10-2), sodium sulfide ( $\text{Na}_2\text{S}$ ) (CAS# 1313-82-2), zirconium(IV) chloride ( $\text{ZrCl}_4$ ) (CAS# 10026-11-6), and polyvinylidene fluoride (PVDF)  $(-\text{C}_2\text{H}_2\text{F}_2)_n-$  (CAS# 24937-79-9) from Sigma-Aldrich. Merck supplied dimethylformamide (DMF) (CAS # 68-12-2), *N*-methyl-2-pyrrolidone (NMP) (CAS# 872-50-4), and benzene-1,4-dicarboxylic acid (terephthalic acid) ( $\text{C}_6\text{H}_4(\text{CO}_2\text{H})_2$ ) (CAS# 100-21-0). Powdered activated carbon was sourced from Duksan Pure Chemicals. Ethanol ( $\text{C}_2\text{H}_5\text{OH}$ ) (CAS# 64-17-5) was obtained from BDH, and deionized water was obtained from the Vitro diagnostics laboratory.

## 2.2 Synthesis of pure $\text{WS}_2$

The  $\text{WS}_2$  bulk nanosheets were prepared by analytical grade  $\text{Na}_2\text{WO}_4 \cdot 2\text{H}_2\text{O}$  and  $\text{Na}_2\text{S}$  in a hydrothermal process with no additional purification. Quantities of 20 mmol  $\text{Na}_2\text{WO}_4 \cdot 2\text{H}_2\text{O}$  and 20 mmol  $\text{Na}_2\text{S}$  were mixed in 50 mL distilled water and constantly agitated for 30 minutes to generate a clear solution in a conventional synthesis. This mixture was introduced to a stainless-steel autoclave lined with Teflon and heated to 220 °C for the duration of 6 h. The prepared powder was then washed and separated *via* centrifugation several times with ethanol and DI water. The bulk sheets were then obtained after vacuum drying at 70 °C. The prepared nanosheets were then exfoliated with the help of probe sonication for 6 hours to obtain the exfoliated nanosheets of pure  $\text{WS}_2$ .

## 2.3 Synthesis of $\text{WS}_2/\text{UiO-66}$ hybrids

A one-pot solvothermal synthesis was used to synthesize  $\text{WS}_2$  and MOF hybrids at various concentrations. Exfoliated  $\text{WS}_2$  and  $\text{ZrCl}_4$  were added to a solution of BDC, DMF, and acetic acid in different weight percent ratios (1:1, 1:2, 1:3). For full inclusion of the reactants, the solution was agitated for 30 minutes and then sonicated for 2 hours. The mixtures underwent a 24 hour heating process in a Teflon-lined stainless-steel autoclave at 120 °C. Once the reaction period concluded, the autoclave was cooled to room temperature. Centrifugation was used to separate the solid product, which was washed thrice with DMF and ethanol. Finally, the obtained powder was dried overnight at 70 °C.

## 2.4 Bulk and exfoliated $\text{WS}_2$

The primary distinction between bulk  $\text{WS}_2$  and exfoliated  $\text{WS}_2$  is in the form of monolayers or few-layer nanosheets, which influence the electrical and structural properties. Exfoliation of  $\text{WS}_2$  refers to the process of separating the three-dimensional layered structure of bulk  $\text{WS}_2$  to produce individual or a few layers of  $\text{WS}_2$ . As more catalytic active sites are exposed, the surface area increases considerably. When  $\text{WS}_2$  is exfoliated into monolayers or few layers, the electrical characteristics of the material, such as the temperature-dependent resistivity, contact resistance, band structure, and electronic excitation, can change dramatically.<sup>43,44</sup> Exfoliated  $\text{WS}_2$  has been shown to have greater electrical conductivity than its bulk form. Exfoliated  $\text{WS}_2$  was found to be highly conductive at room temperature, with values of around  $7 \text{ S cm}^{-1}$ , which is an order of

magnitude higher than the conductivity of bulk  $\text{WS}_2$  evaluated under similar conditions.<sup>45</sup>

Electrical conductivity is critical for electrode electrocatalytic activity in water splitting reactions. A high electrical conductivity of the electrode material increases charge transfer at the electrode–electrolyte interface, hence speeding up the electrocatalytic reactions involved in the water splitting process. This leads to faster reaction times and lower overpotentials. Furthermore, electrodes with high electrical conductivity help to reduce ohmic losses and, as a result, energy consumption during water splitting.<sup>46,47</sup>

## 2.5 Electrocatalysts characterization

An X-ray diffractometer was used to perform compositional analyses and phase studies on the developed catalyst (XRD; STOE Germany). The  $2\theta$  range for the test was 10°–90°, and Cu-K radiation was used. SEM (JEOL-instrument JSM-6490A) was used to study and investigate the catalyst's structure and morphology and the lattice structure. Brunauer–Emmett–Teller (BET) was performed to evaluate the pore size distribution and available active surface.

## 2.6 Electrochemical study

The electrocatalytic activity was determined under ambient conditions using a three-electrode cell configuration. 1.0 M KOH was used as an electrolyte. The counter electrode was composed of Pt-wire. Ag/AgCl is preferred as a reference electrode in water-splitting experiments because it is highly stable in aqueous solutions, and does not undergo significant changes in potential over time. It also has a well-defined and known standard potential with easily reproducible results. The working electrode was constructed of the catalyst on Ni-foam. For calculations following the formula, the potential was changed to a reversible hydrogen electrode (RHE) for the standardization equation.

$$E_{\text{RHE}} = E_{\text{Ag/AgCl}} + 0.059 \text{ pH} + E_{\text{Ag/AgCl}}^0 \quad (1)$$

where  $\text{pH} = 14$ ;  $E_{\text{Ag/AgCl}}^0 = 0.1976$ .

The electrocatalysts' performance was assessed through several techniques, including cyclic voltammetry (CV), linear sweep voltammetry (LSV), electrochemical impedance spectroscopy (EIS), and chronopotentiometry. For the linear sweep voltammetry (LSV) analysis, a scan rate of  $10 \text{ mV s}^{-1}$  was used within a potential range of 0 to 1.5 V. Cyclic voltammetry measurements were conducted within the potential range of 0 to 0.6 V, employing various scan speeds (10, 20, 50, 100, 150), and the results were reported at  $50 \text{ mV s}^{-1}$ . Tafel plots were generated, where the y-axis represented the overpotential, and the x-axis displayed the logarithm of the current density. The slope of the Tafel plots was determined using a linear equation (eqn (2)).

$$\eta' = m \log j + a \quad (2)$$

where  $\eta'$  = overpotential;  $m$  = Tafel slope;  $j$  = current density;  $a$  = Tafel constant.



In electrochemical impedance spectroscopy (EIS), the frequency range utilized was from 0.1 Hz to 2 MHz, with an alternating voltage amplitude of 10 mV. To assess the stability of the electrocatalyst, chronopotentiometry was employed. In chronopotentiometry, the rate of the potential change over time was calculated while maintaining a constant current of  $10 \text{ mA cm}^{-2}$ . Frequently, stability curves were supplied within 24 hours.

### 3. Results and discussion

#### 3.1 X-ray<sub>kα</sub> diffraction

Fig. 1 displays the XRD pattern of all the prepared samples. Fig. 1(a) reveals the pure and well-formed crystalline peaks of tungsten disulfide nanosheets at  $14.36^\circ$ ,  $32.76^\circ$ ,  $39.59^\circ$ ,  $44.05^\circ$ ,  $49.79^\circ$ , and  $58.49^\circ$ , which are analogous to the diffraction planes of (002), (100), (103), (006), (105) and (110), respectively. These patterns are well matched with the XRD patterns of

the conventional  $\text{WS}_2$  having a hexagonal lattice (JCPDS: 84-1398).<sup>48</sup>

Other modest diffractions were seen in the (100), (103), (105), and (110) planes. For the hexagonal phase, the diffractions and peak intensities correspond well with the standard JCPDS (JCPDS 08-0237) database.<sup>49</sup> UiO-66 was effectively synthesized, as evidenced by the emergence of three distinct peaks at  $2\theta = 7.38^\circ$ ,  $8.56^\circ$ , and  $25.67^\circ$ .<sup>50</sup> Any defect in its crystal-line structure is not visible. All of the hybrids display the characteristic UiO-66 peaks corresponding to the crystallographic planes (111) and (002) at  $7.2^\circ$  and  $8.0^\circ$ , respectively. Moreover, the crystallite size is calculated using the Scherrer formula given in eqn (3).<sup>51</sup>

$$D = k\lambda / (\text{FWHM}) \times (\cos \theta) \quad (3)$$

In the above equation, FWHM is the integral width (it is the area under the curve divided by the maximal height, taken in radians),  $D$  is the apparent size of the crystal, and  $k$  is a constant

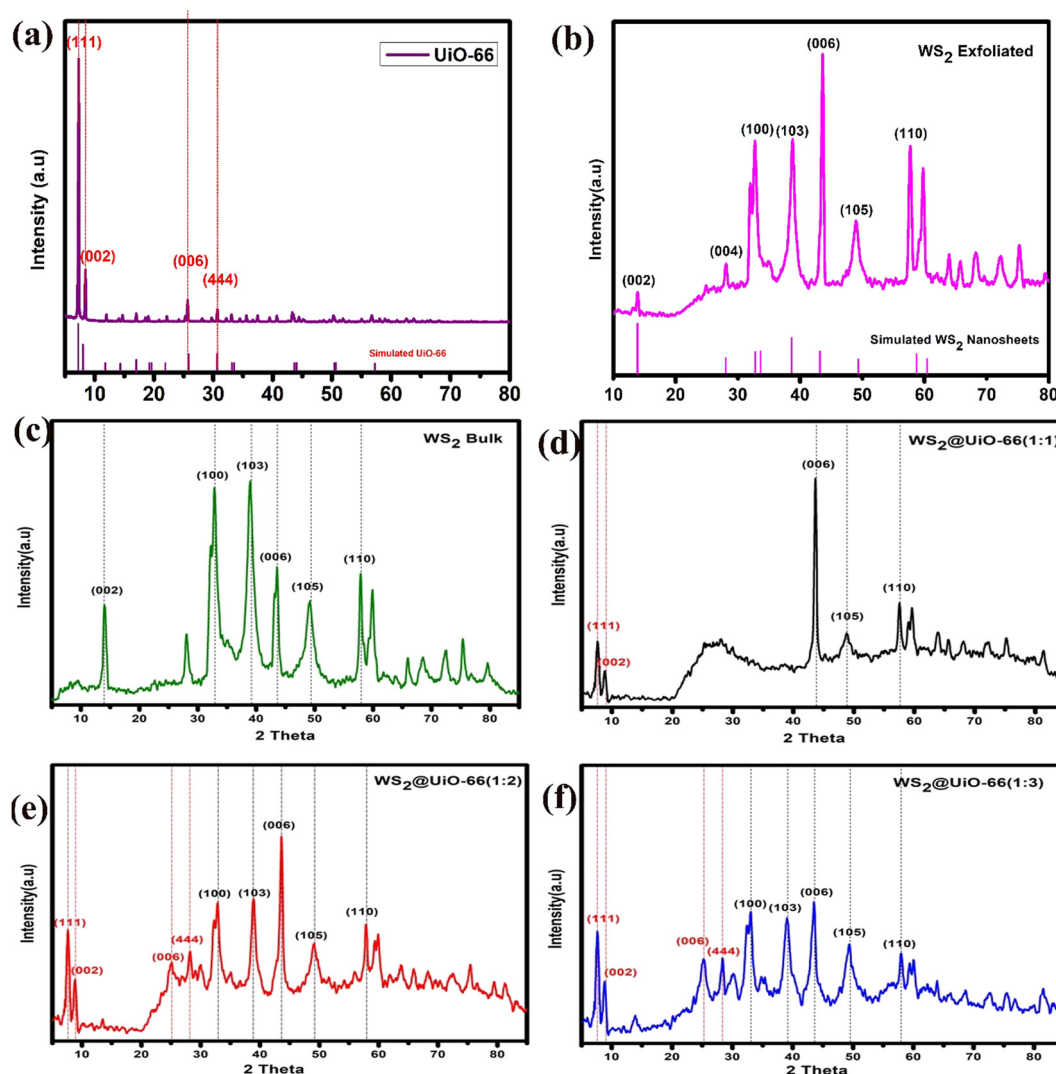


Fig. 1 Powder X-ray<sub>kα</sub> diffractometry: (a) pure UiO-66, (b) exfoliated  $\text{WS}_2$ , (c) bulk  $\text{WS}_2$ , (d)  $\text{WS}_2$ @UiO-66(1:1), (e)  $\text{WS}_2$ @UiO-66(1:2), (f)  $\text{WS}_2$ @UiO-66(1:3).





with a value near 1 (*i.e.*, 0.94), Cu-K $\alpha$  1.54 is the X-ray<sub>K $\alpha$</sub>  wavelength, and  $\theta$  is the Bragg angle. An average crystal size of 240 Å (24 nm) of the bulk tungsten disulfide was calculated using the Scherrer calculator, exfoliated WS<sub>2</sub> is 277 Å (27.7 nm), WS<sub>2</sub>@UiO-66(1:1) is 244 Å (24.4 nm), WS<sub>2</sub>@UiO-66(1:2) is 234.5 Å (23.45 nm), WS<sub>2</sub>@UiO-66(1:3) is 179 Å (17.9 nm) and pure UiO-66 is 172 Å (17.2 nm). The XRD graphs of bulk WS<sub>2</sub> and exfoliated WS<sub>2</sub> show that bulk WS<sub>2</sub> has broader peaks than exfoliated WS<sub>2</sub>, which is why bulk WS<sub>2</sub> has a greater FWHM value and smaller crystallite size than exfoliated WS<sub>2</sub>. To create hybrids, exfoliated WS<sub>2</sub> with a crystallite size of 27.7 nm was utilized. As the concentration of UiO-66 in the hybrids increased, the crystallite size was notably reduced. This can be ascribed to the smaller crystallite size and higher concentration of UiO-66. The peaks observed in WS<sub>2</sub>@UiO-66(1:3) are wider than those in WS<sub>2</sub>@UiO-66(1:2) due to this effect. Consequently, WS<sub>2</sub>@UiO-66(1:3) has a smaller crystallite size compared to all of the other hybrids.

### 3.2 Scanning electron microscope (SEM)

The microstructures of the synthesized material were observed *via* SEM examination. Irregular nanosheets of the synthesized WS<sub>2</sub> are produced, as shown in Fig. 2(a) and (b). Based on the SEM morphology of WS<sub>2</sub>@UiO-66(1:1), the two structures may be fused to generate shapeless nanoparticles, with no single morphology of either structure dominating, which is also due to aggregation. Although certain particles can be observed embedded in the structure, there is no way to tell them apart. This method of synthesis resulted in a chaotic structure with aggregated particles. UiO-66 structures formed in clusters can be seen in WS<sub>2</sub>@UiO-66(1:2) (Fig. 2(d)). It is possible that the UiO-66 polyhedral was formed on the WS<sub>2</sub> sheets as a

foundation. UiO-66 has difficulty developing a stable crystalline structure.<sup>52</sup> The morphologies of the UiO-66 samples described in the literature generally have irregular intergrown microcrystalline polyhedral shapes.<sup>7,53</sup>

### 3.3 EDX

Fig. 3(a) display the EDX plots for the hybrid WS<sub>2</sub>@UiO-66(1:2), revealing the presence of all of the crucial elements, such as Tungsten, Sulphur, Zirconium, Carbon, and Oxygen, as indicated by the corresponding ratios in the inset. It needs to be mentioned that the composition was uniform throughout the samples. The EDX elemental analysis serves as additional confirmation of the successful synthesis of the UiO-66 and WS<sub>2</sub> hybrid.

### 3.4 BET

Nitrogen adsorption was used to measure the surface area of the structure. Many properties can be determined using the pore size distribution curves and BET analysis, like the pore size distribution, pore volume of the hybrid, and surface area, as shown in Fig. 4(a) and (b). According to the Brunauer–Deming–Deming Teller classification, the isotherm produced for WS<sub>2</sub>@UiO-66(1:2) is of type IV. The WS<sub>2</sub>@UiO-66(1:2) nanosheets had a pore volume, pore diameter, and surface area of 0.23165 cm<sup>3</sup> g<sup>−1</sup>, 4.9 nm, and 125.06 m<sup>2</sup> g<sup>−1</sup>, respectively, which is very large compared to the previously reported WS<sub>2</sub> nanosheets (pore volume is 0.067 cm<sup>3</sup> g<sup>−1</sup>, and surface area of 65.05 m<sup>2</sup> g<sup>−1</sup>, respectively).<sup>54</sup> Because the prepared materials have a large surface area, the synthesized material might have many available sites on the surface and help with electrolyte interaction.

## 4. Electrochemical study

### 4.1 Hydrogen evolution reaction (HER)

Fig. 5(a) illustrates the electrocatalytic HER performance curves for bulk WS<sub>2</sub>, exfoliated WS<sub>2</sub>, WS<sub>2</sub>@UiO-66(1:3), WS<sub>2</sub>@UiO-66(1:2), and WS<sub>2</sub>@UiO-66(1:1). Part (a) of Fig. 5 shows the LSV charts of all materials determined in 1.0 M KOH, with an applied potential range from 0 to −1.5 V and sweep rate of 10 mV s<sup>−1</sup>. LSV is a metric for the electroactive substances' chemical reactivity. The overpotential plays a crucial role in assessing the potential of a catalyst for water-splitting. It refers to the potential applied beyond the equilibrium potential to initiate the reaction and facilitate the release of entities at the electrodes. The calculation of the overpotential at a specific current density allows for the evaluation of the electrode's activity. A lower overpotential indicates a higher electrochemical activity of the catalyst. As a standard practice, the overpotential is measured and compared at a current density of 10 mA cm<sup>−2</sup> for all prepared catalysts.<sup>43</sup> At the current density of 100 mA cm<sup>−2</sup>, WS<sub>2</sub> bulk, exfoliated WS<sub>2</sub>, WS<sub>2</sub>@UiO-66(1:1), and WS<sub>2</sub>@UiO-66(1:3) demonstrated HER overpotentials of 149 mV, 153 mV, 123 mV, and 136 mV, respectively. WS<sub>2</sub>@UiO-66(1:2) demonstrated improved HER activity as compared to pure compounds and other hybrids with a small

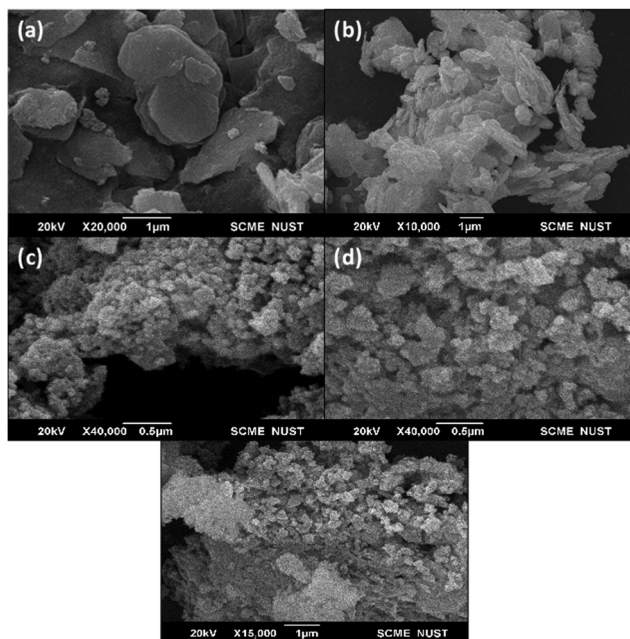


Fig. 2 SEM images of (a) bulk WS<sub>2</sub>, (b) exfoliated WS<sub>2</sub>, (c) WS<sub>2</sub>@UiO-66(1:1), (d) WS<sub>2</sub>@UiO-66(1:2), (e) WS<sub>2</sub>@UiO-66(1:3).



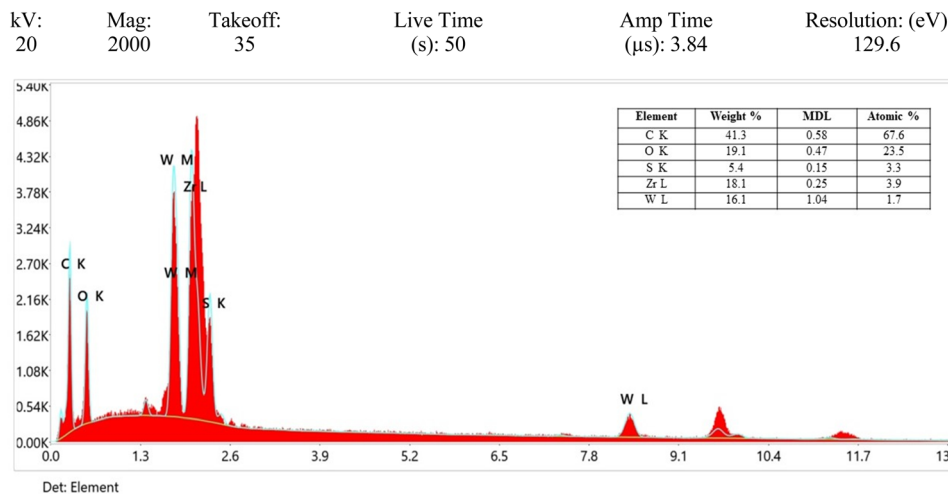


Fig. 3 EDX analysis of hybrid  $\text{WS}_2@\text{UiO}-66(1:2)$ .

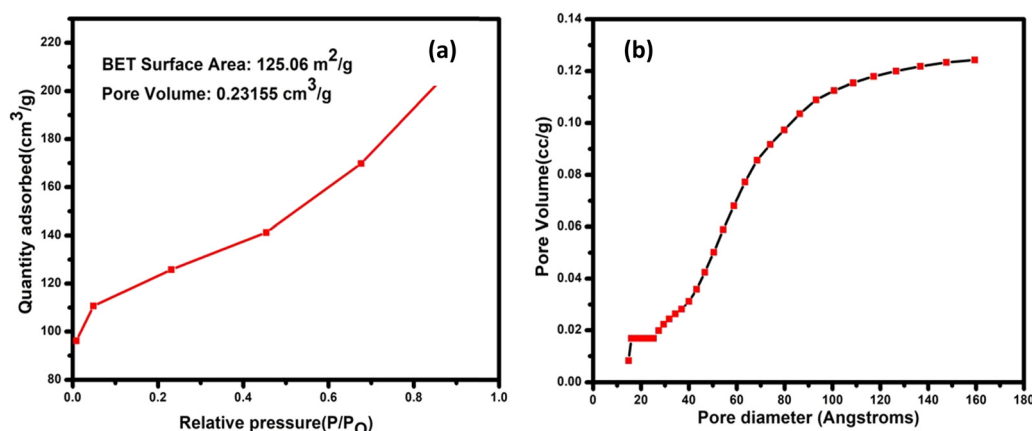


Fig. 4 (a) BET adsorption isotherm and the (b) pore size distribution curve.

overpotential of 121 mV at a current density of  $10 \text{ mA cm}^{-2}$ . The Tafel plots show how the overpotential response rate is related. The Tafel slope in Fig. 5(b) can be used to deduce the reaction mechanism and check the activity in the HER.

The Tafel plot of HER might give the rate-limiting phase. The electron transport is faster in the sample with a low Tafel plot. So, achieving a high current density and low Tafel slope is needed, along with a low overpotential. The bulk  $\text{WS}_2$ , exfoliated  $\text{WS}_2$ ,  $\text{WS}_2@\text{UiO}-66(1:1)$ , and  $\text{WS}_2@\text{UiO}-66(1:3)$  had Tafel values of  $163 \text{ mV dec}^{-1}$ ,  $298 \text{ mV dec}^{-1}$ ,  $115 \text{ mV dec}^{-1}$ , and  $113 \text{ mV dec}^{-1}$ , respectively, whereas  $\text{WS}_2@\text{UiO}-66(1:2)$  had the lowest Tafel value of  $83 \text{ mV dec}^{-1}$ . A high Tafel value denotes a high charge transfer resistance, while a low Tafel value denotes a quick hydrogen production rate. After a 24 hour chronopotentiometry test,  $\text{WS}_2@\text{UiO}-66(1:2)$  exhibits HER stability with a small reduction in performance.  $\text{WS}_2@\text{UiO}-66(1:2)$ , in conclusion, delivers the highest production for HER electrocatalytic water-splitting and is comparable to several previously reported highly efficient catalysts (Table 3). The increased surface area, synergistic effects amongst metals, and

the presence of conductive channels provided by the MOF network all contribute to the increased performance. Bimetallic catalysts often outperform catalysts composed of a single metal component due to various factors. These include synergistic effects, structural and composition-dependent enhancements in the active sites, and the ability to improve the current density and over-potential characteristics in the water oxidation process. The presence of a larger number of accessible catalytic sites, along with an open structure and bimetallic synergy, promotes rapid mass movement and enhances electron transmission.<sup>55</sup> The more negative conduction band potential of  $\text{WS}_2$  compared to UiO-66 facilitates the rapid and efficient flow of electrons from  $\text{WS}_2$  to UiO-66, thereby enhancing the process of water splitting. The covalent interaction between  $\text{WS}_2$  and UiO-66 leads to the formation of heterojunctions, enabling swift electron transfer and consequently enhancing the HER.

#### 4.2 Oxygen evolution reaction (OER)

Fig. 6(a) shows the LSV polarization curves used to assess the OER activity of the prepared electrocatalysts in 1.0 M KOH,



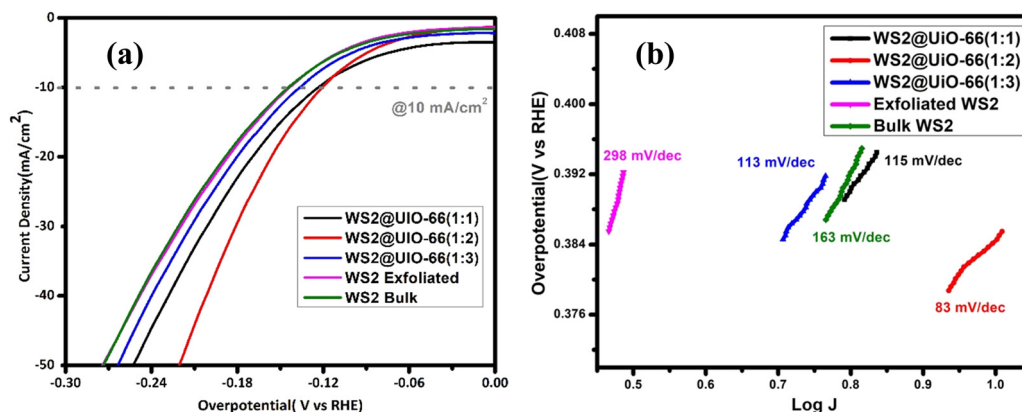


Fig. 5 (a) LSV HER curves of bulk WS<sub>2</sub>, exfoliated WS<sub>2</sub>, and WS<sub>2</sub>@UiO-66(1:1, 1:2, and 1:3) at a scan rate of 10 mV s<sup>-1</sup> in 1.0 M KOH. (b) Corresponding Tafel plots of bulk WS<sub>2</sub>, exfoliated WS<sub>2</sub> and WS<sub>2</sub>@UiO-66(1:1, 1:2, 1:3).

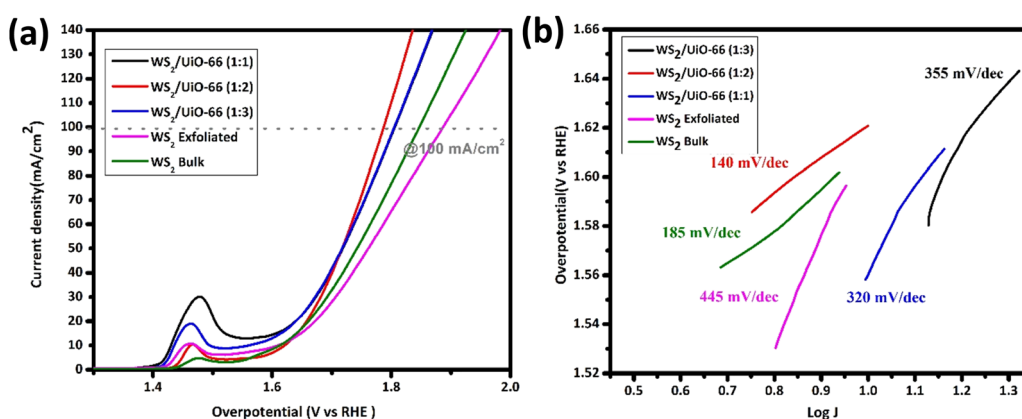


Fig. 6 (a) LSV OER curves of bulk WS<sub>2</sub>, exfoliated WS<sub>2</sub>, WS<sub>2</sub>@UiO-66(1:1, 1:2, 1:3) at a scan rate of 10 mV s<sup>-1</sup> in 1.0 M KOH. (b) Corresponding Tafel plots of bulk WS<sub>2</sub>, exfoliated WS<sub>2</sub> and WS<sub>2</sub>@UiO-66(1:1, 1:2, 1:3).

applied potential range from 0 to 1.5 V and sweep rate of 10 mV s<sup>-1</sup>. An anodic peak near 1.45 V is observed. This peak is mainly attributed to the change in the electronic state of the involved metals *via* oxidation. It is an acceptable practice to compare and use a higher overpotential point to compensate for the offset effect of the oxidation peaks. Since the oxidation reaction has occurred and the state of the metal is changed, this changed electronic configuration will now take part in the OER.<sup>56–62</sup> The overpotential is measured and compared at 100 mA cm<sup>-2</sup>. WS<sub>2</sub>@UiO-66(1:2) requires an overpotential of around about 550 mV to attain 100 mA cm<sup>-2</sup> current density, which is less than bulk WS<sub>2</sub> (650 mV), exfoliated WS<sub>2</sub> (610 mV), WS<sub>2</sub>@UiO-66(1:1) (570 mV), and WS<sub>2</sub>@UiO-66(1:3) (570 mV). Fig. 6(b) shows a Tafel diagram of the OER reaction kinetics. In comparison to bulk WS<sub>2</sub> (198 mV dec<sup>-1</sup>), exfoliated WS<sub>2</sub> (206 mV dec<sup>-1</sup>), WS<sub>2</sub>@UiO-66(1:1) (191 mV dec<sup>-1</sup>), WS<sub>2</sub>@UiO-66(1:3) (186 mV dec<sup>-1</sup>) and WS<sub>2</sub>@UiO-66(1:2) (136 mV dec<sup>-1</sup>), WS<sub>2</sub>@UiO-66(1:2) exhibits the smallest Tafel slope at 136 mV dec<sup>-1</sup>. The OER and HER results are summarized in Table 1.

WS<sub>2</sub>@UiO-66(1:2) offers the highest production for the HER and OER electrocatalytic water-splitting, and is comparable to

several highly effective catalysts that were previously reported (Table 2). The higher surface area and the efficient electron transport networks with the appearance of conducting passageways supplied by the MOF network are responsible for the enhanced performance. EIS is yet another parameter that is important for the understanding of the kinetic mode of the prepared catalyst. The frequency range used for EIS was 200 kHz–0.1 Hz. Fig. 7(a) demonstrates a Nyquist plot with actual impedance on the x-axis and fictitious impedance on the y-axis. The Nyquist plot, which has a simple Randles circuit, gives information on the charge transfer resistance ( $R_{ct}$ ), solution resistance ( $R_s$ ), and faradaic capacitance at the electrode/electrolyte interface ( $C_f$ ). Table 2 shows the comparative values. In general, small charge transfer resistance ( $R_{ct}$ ) values are associated with rapid charge transfer kinetics.<sup>2,63</sup>

In comparison, WS<sub>2</sub>@UiO-66(1:2) exhibits an interface between the catalyst and electrolyte with the lowest charge transfer resistance. Rapid kinetics is proposed by the tiny  $R_{ct}$  of WS<sub>2</sub>@UiO-66(1:2), which corresponds with the Tafel slope attributes and LSV results. Electrochemical active surface area (ECSA) is an excellent method for determining the catalyst



Table 1 Summary of the HER and OER

Electrocatalysts	Overpotential HER (mV at 10 mA cm <sup>-2</sup> )	Tafel slope HER (mV dec <sup>-1</sup> )	Overpotential OER (mV at 100 cm <sup>2</sup> )	Tafel slope OER (mV dec <sup>-1</sup> )
Bulk WS <sub>2</sub>	149	163	650	198
Exfoliated WS <sub>2</sub>	153	283	610	206
WS <sub>2</sub> @UiO-66(1 : 1)	123	115	570	191
WS <sub>2</sub> @UiO-66(1 : 2)	121	83	550	136
WS <sub>2</sub> @UiO-66(1 : 3)	136	113	570	186

Table 2 Comparative values of  $R_{ct}$ ,  $R_s$ , and ECSA

Electrocatalyst	$R_{ct}$ (Ohms)	$R_s$ (Ohms)	ECSA (cm <sup>2</sup> )
Bulk WS <sub>2</sub>	220	3.05	356
Exfoliated WS <sub>2</sub>	160	2.8	507.5
WS <sub>2</sub> @UiO-66(1 : 1)	5.4	2	1106
WS <sub>2</sub> @UiO-66(1 : 2)	2.65	2.45	1262.5
WS <sub>2</sub> @UiO-66(1 : 3)	9.895	2.75	957.5

activity. Electrocatalysts with higher ECSAs require lower reaction overpotentials. ECSA is calculated by determining the double-layer capacitance ( $C_{dl}$ ) using eqn (4) and (5).<sup>64</sup>

$$ECSA = C_{dl}/C_f \quad (4)$$

$$C_{dl} = \frac{(Y_0^* R_p)^{1/\alpha}}{R_p} \quad (5)$$

$C_{dl}$  = double-layer capacitance,  $C_f$  = specific capacitance of an ideal flat surface catalyst known as individual capacitance

(average value of 40 F cm<sup>-2</sup>),  $Y_0$  = magnitude of capacity (dimensionless measure indicating the extent to which a catalyst diverges from a genuine capacitor),  $R_p$  = polarization resistance.

To check the cyclic stability of the prepared hybrid, cyclic voltammetry of WS<sub>2</sub>@UiO-66(1 : 2) was done at various scan rates. Fig. 7(b) demonstrates a steady increase in the exchange current density when the voltage is increased, indicating the cyclic stability, strong electrocatalyst efficiency, low resistance of the prepared catalysts, and a considerable drop in the charge transfer resistance as the potential is increased. CV measurements of the bulk WS<sub>2</sub>, exfoliated WS<sub>2</sub>, and WS<sub>2</sub>@UiO-66(1 : 1, 1 : 2, 1 : 3) were carried out at 100 mV s<sup>-1</sup> scan rate in 1.0 M KOH electrolyte solution to identify the relationship between the current density and voltage over a range (Fig. 7(c)). The CV graphs provide information on the redox reaction thermodynamics and the electron-transfer reaction kinetic model. The CV curves reveal two well-defined redox peaks. In

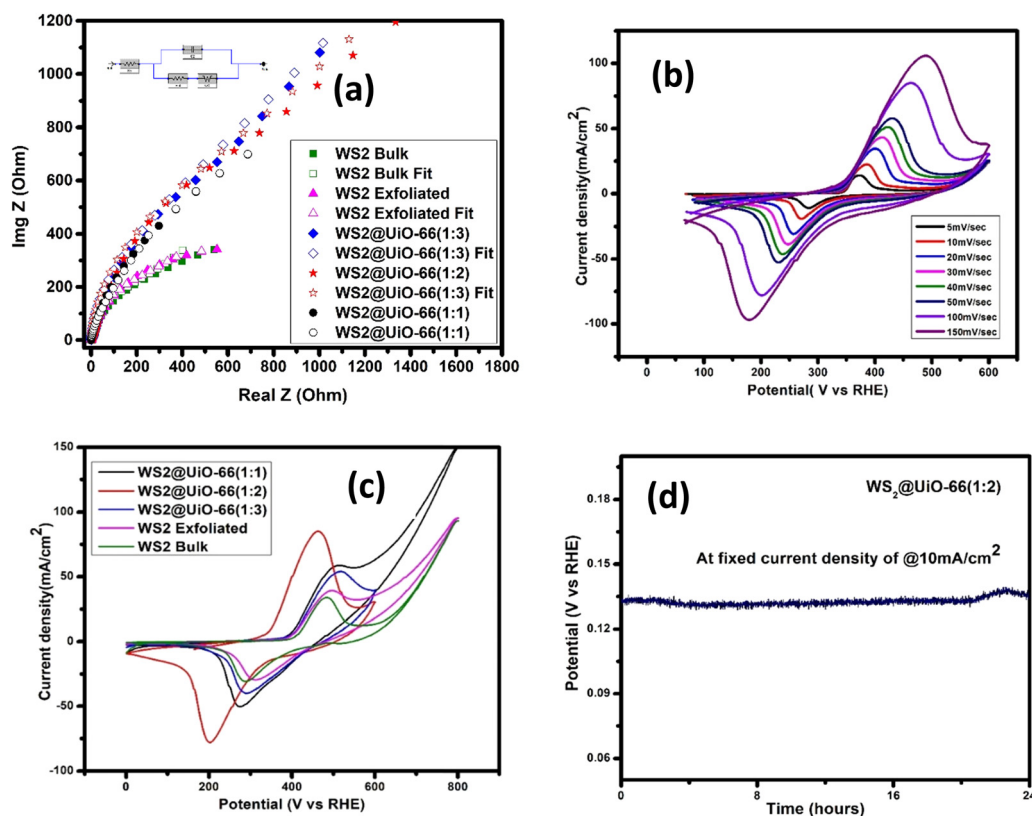


Fig. 7 (a) EIS Nyquist plots of all the prepared hybrids with fitted curves. (b) CV of WS<sub>2</sub>@UiO-66(1 : 2) at different scan rates. (c) CV of all the prepared hybrids at a scan rate of 50 mV s<sup>-1</sup>. (d) Stability test at a fixed current density of 10 mA cm<sup>-2</sup>.



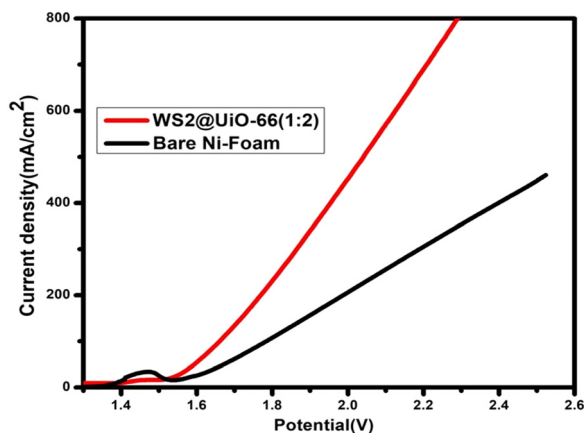


Fig. 8 The bifunctional overall cell performance of  $\text{WS}_2/\text{UiO}-66(1:2)$  and bare-Ni foam electrocatalysts.

comparison,  $\text{WS}_2/\text{UiO}-66(1:2)$  has a larger current density, implying lower diffusion layer resistance and cyclic stability. The charge that travels through the cell is equivalent to the current density. Furthermore, the catalyst's durability is crucial for commercializing hydrogen production as a fuel concept. Fig. 7(d) shows the stability of  $\text{WS}_2/\text{UiO}-66(1:2)$  after 24 hours of testing. The potential response remained consistent after the  $\text{WS}_2/\text{UiO}-66(1:2)$  catalyst was activated, with no significant reduction in activity. A bifunctional electrocatalytic cell was constructed to evaluate the hybrid  $\text{WS}_2/\text{UiO}-66(1:2)$  ability to split water. In this two-electrode assembly,  $\text{WS}_2/\text{UiO}-66(1:2)$  on the Ni-foam acted as both cathode and anode in 1.0 M KOH. Bare Ni-foam was also investigated under similar process conditions (results are shown in Fig. 8). To achieve a current density of  $10 \text{ mA cm}^{-2}$ , an electrolyzer cell voltage of 1.41 Volts was required, which is significantly lower than the standard  $\text{Pt/C}||\text{IrO}_2$  with an electrolysis potential of 1.60 V<sup>65</sup> and several other reported bifunctional water-splitting electrocatalysts mentioned in Table 3.

The improved performance of the  $\text{WS}_2$  and UiO-66 hybrids as electrocatalysts for water splitting, compared to pristine  $\text{WS}_2$ , can be attributed to several key factors. Hybrid catalysts, consisting of a combination of different metal components (Tungsten in  $\text{WS}_2$  and Zirconium in UiO-66), have demonstrated superior performance compared to single metal catalysts. The diverse metal sites in the hybrid catalyst can facilitate

multiple reaction pathways, leading to improved catalytic activity. Synergistic interactions between  $\text{WS}_2$  and UiO-66 lead to improved charge transfer kinetics, reducing overpotentials for these reactions. Additionally, the hybrid's unique structural features, such as increased surface area and enhanced electron mobility, further enhance its electrocatalytic properties. These hybrids can significantly enhance the catalytic activity of  $\text{WS}_2$  by providing additional active sites for HER and OER.

Certain parameters need to be addressed that limit large-scale applications. High catalyst loading is often required to achieve efficient water splitting, which can be challenging on a large scale. Ensuring efficient mass transport of reactants (water, protons, etc.) to the catalytic sites and removal of products (hydrogen and oxygen) can be challenging, especially at large scales. The reproducible synthesis of high-quality electrocatalysts can be complex. Scaling up the production of such catalysts while maintaining their quality can be a challenge. The kinetics of the HER may not be as fast as desired on a larger scale, leading to lower reaction rates.

## 5. Conclusions

This work demonstrates the one-pot solvothermal method used to produce the 2D bifunctional tungsten disulfide embedded with UiO-66 ( $\text{WS}_2/\text{UiO}-66$ ) hybrids, and how their structure affects its properties and performance of water splitting. The results also showed that using different reactants and reaction conditions for hybrid production results in varied interactions between  $\text{WS}_2$  and UiO-66. As a result, the catalysts' morphological geometry and electrocatalytic characteristics are affected.  $\text{WS}_2/\text{UiO}-66(1:2)$  demonstrated exceptional electrocatalytic activity, achieving a current density of  $10 \text{ mA cm}^{-2}$  with a HER overpotential of 121 mV and OER overpotential of 220 mV. The  $\text{WS}_2/\text{UiO}-66(1:2)$  maintains its stability after 24 hours, so this electrocatalyst is very suitable for commercialization. The increased surface area, metal synergistic effects, excellent electron transport route adjustment, and the MOF network's presence of conductive pathways all contribute to the enhanced performance. These discoveries lay the foundation for the design and production of bifunctional hybrid electrocatalysts in water-splitting devices. To develop a better understanding of the catalyst, a deeper understanding of the molecular level of process kinetics, the electron transfer mechanism, and the structural information of electrocatalysts is required.

Table 3 Comparisons of the HER and OER electrocatalyst activity with previously reported catalysts

Electrocatalysts	Current density ( $\text{mA cm}^{-2}$ )	Overpotential HER (mV)	Overpotential OER (mV)	Stability (hours)	Ref.
$\text{WS}_2/\text{UiO}-66(1:2)$	10	121	220	24	This work
$\text{MoS}_2/\text{UiO}-66$	10	129.4	180	24	7
$\text{CoO}_x/\text{UiO}-66-300$	10	—	283	10	66
$\text{WS}_2/\text{Co}_3\text{S}_4 \text{ NW/CC}$	10	82	280	24	1
$\text{Ag}/\text{WS}_2$	10	180	—	24	67
$\text{WS}_2\text{-Co}$	10	210	—	24	68
$\text{Ni}/\text{WS}$	8.6	250	—	24	69
$\text{W}_{1-x}\text{S}_2\text{-Mo}_x/\text{CFP}$	10	178	—	18	70
$\text{WS}_2/\text{Co}(1-x)_2 \text{ S, N}$	10	220	365	—	71



## Conflicts of interest

The authors declare no deliberate competing interests regarding research, financial benefit, authorship, and/or publication that could have influenced this paper.

## Acknowledgements

The Higher Education Commission of Pakistan funded this work under the grant allocated as 2017/HEC/NRPU-10482.

## References

- 1 T. Zhang, *et al.*, Bifunctional WS<sub>2</sub>@Co<sub>3</sub>S<sub>4</sub> core-shell nanowire arrays for efficient water splitting, *Electrochim. Acta*, 2022, **404**, 139648.
- 2 U. Abdullah, M. Ali and E. Pervaiz, An inclusive review on recent advancements of cadmium sulfide nanostructures and its hybrids for photocatalytic and electrocatalytic applications, *Mol. Catal.*, 2021, **508**, 111575.
- 3 R. Kumar, *et al.*, Strong interactions between the nanointerfaces of silica-supported Mo<sub>2</sub>C/MoP heterojunction promote hydrogen evolution reaction, *ACS Appl. Mater. Interfaces*, 2020, **12**(52), 57898–57906.
- 4 Z. Pu, *et al.*, Single-atom catalysts for electrochemical hydrogen evolution reaction: recent advances and future perspectives, *Nano-Micro Lett.*, 2020, **12**(1), 1–29.
- 5 U. Abdullah, M. Ali and E. Pervaiz, Cadmium sulfide embedded Prussian Blue as highly active bifunctional electrocatalyst for water-splitting process, *Int. J. Hydrogen Energy*, 2022, **47**(49), 21160–21172.
- 6 H. Hosseini and M. Roushani, Rational design of hollow core-double shells hybrid nanoboxes and nanopipes composed of hierarchical Cu-Ni-Co selenides anchored on nitrogen-doped carbon skeletons as efficient and stable bifunctional electrocatalysts for overall water splitting, *Chem. Eng. J.*, 2020, **402**, 126174.
- 7 M. Ali and E. Pervaiz, Effect of synthesis route on electrocatalytic water-splitting activity of MoS<sub>2</sub>/UiO-66 hybrid, *Mol. Catal.*, 2022, **519**, 112136.
- 8 P. Chen, *et al.*, Recent progress of transition metal carbides/nitrides for electrocatalytic water splitting, *J. Alloys Compd.*, 2021, **883**, 160833.
- 9 S. Tang, *et al.*, Recent advances in transition metal nitrides for hydrogen electrocatalysis in alkaline media: From catalyst design to application, *Front. Chem.*, 2022, **10**, 1073175.
- 10 T. Wang, *et al.*, Precious metal-free approach to hydrogen electrocatalysis for energy conversion: From mechanism understanding to catalyst design, *Nano Energy*, 2017, **42**, 69–89.
- 11 J. Yang, *et al.*, From hexagonal to monoclinic: engineering crystalline phase to boost the intrinsic catalytic activity of tungsten oxides for the hydrogen evolution reaction, *ACS Sustainable Chem. Eng.*, 2021, **9**(16), 5642–5650.
- 12 J. Hei, *et al.*, NiFeP nanosheets on N-doped carbon sponge as a hierarchically structured bifunctional electrocatalyst for efficient overall water splitting, *Appl. Surf. Sci.*, 2021, **549**, 149297.
- 13 T. S. ZelekeA, *et al.*, Immobilized single molecular molybdenum disulfide on carbonized polyacrylonitrile for hydrogen evolution reaction, *ACS Nano*, 2019, **13**(6), 6720–6729.
- 14 U. Abdullah, *et al.*, An inclusive perspective on the recent development of tungsten-based catalysts for overall water-splitting: A review, *Int. J. Energy Res.*, 2022.
- 15 X. Chen, *et al.*, Design principles for tungsten oxide electrocatalysts for water splitting, *ChemElectroChem*, 2021, **8**(23), 4427–4440.
- 16 Z. Feng, *et al.*, Controllable synthesis of flower-like Mn-Co-P nanosheets as bifunctional electrocatalysts for overall water splitting, *Colloids Surf., A*, 2021, **615**, 126265.
- 17 D. R. Paudel, *et al.*, Fe and P doped 1T-phase enriched WS<sub>2</sub>3D-dendritic nanostructures for efficient overall water splitting, *Appl. Catal., B*, 2021, **286**, 119897.
- 18 T. Kou, S. Wang and Y. Li, Perspective on high-rate alkaline water splitting, *ACS Mater. Lett.*, 2021, **3**(2), 224–234.
- 19 B. Zhou, *et al.*, Engineering P-doped Ni<sub>3</sub>S<sub>2</sub>-NiS hybrid nanorod arrays for efficient overall water electrolysis, *J. Alloys Compd.*, 2021, **862**, 158391.
- 20 R. Khan, *et al.*, 3D hierarchical heterostructured LSTN@NiMn-layered double hydroxide as a bifunctional water splitting electrocatalyst for hydrogen production, *Fuel*, 2021, **285**, 119174.
- 21 H. Zhang, *et al.*, Bifunctional heterostructured transition metal phosphides for efficient electrochemical water splitting, *Adv. Funct. Mater.*, 2020, **30**(34), 2003261.
- 22 R. Zhang, *et al.*, Dual synergistic effect of S-doped carbon bridged semi crystalline MILN-based Co<sub>3</sub>S<sub>4</sub>/MnS<sub>2</sub> nanostructure in electrocatalytic overall water splitting, *Electrochim. Acta*, 2021, **366**, 137438.
- 23 Y. Li, *et al.*, Heterostructured MoO<sub>2</sub>@MoS<sub>2</sub>@Co<sub>9</sub>S<sub>8</sub> nanorods as high efficiency bifunctional electrocatalyst for overall water splitting, *Appl. Surf. Sci.*, 2021, **543**, 148804.
- 24 Y. Liu, *et al.*, Hierarchically heterostructured metal hydroxide (oxy) oxides for efficient overall water splitting, *Nanoscale*, 2019, **11**(24), 11736–11743.
- 25 D. Vikraman, *et al.*, Improved Hydrogen Evolution Reaction Performance using MoS<sub>2</sub>-WS<sub>2</sub> Heterostructures by Physicochemical Process, *ACS Sustainable Chem. Eng.*, 2018, **6**(7), 8400–8409.
- 26 W. Yin, *et al.*, Low-temperature one-pot synthesis of WS<sub>2</sub> nanoflakes as electrocatalyst for hydrogen evolution reaction, *Nanotechnology*, 2018, **30**(4), 045603.
- 27 C. Sun, *et al.*, N-doped WS<sub>2</sub> nanosheets: a high-performance electrocatalyst for the hydrogen evolution reaction, *J. Mater. Chem. A*, 2016, **4**(29), 11234–11238.
- 28 F. M. Pesci, *et al.*, MoS<sub>2</sub>/WS<sub>2</sub> heterojunction for photoelectrochemical water oxidation, *ACS Catal.*, 2017, **7**(8), 4990–4998.
- 29 D. Voiry, *et al.*, Enhanced catalytic activity in strained chemically exfoliated WS<sub>2</sub> nanosheets for hydrogen evolution, *Nat. Mater.*, 2013, **12**(9), 850–855.



- 30 T. Van Nguyen, *et al.*, Electrocatalysts based on MoS<sub>2</sub> and WS<sub>2</sub> for hydrogen evolution reaction: An overview, *Battery Energy*, 2023, 20220057.
- 31 Z. Thiehm, A. Shakoor and T. Altahtamouni, Recent advances in WS<sub>2</sub> and its based heterostructures for water-splitting applications, *Catalysts*, 2021, **11**(11), 1283.
- 32 Z. Wu, *et al.*, WS<sub>2</sub> nanosheets as a highly efficient electrocatalyst for hydrogen evolution reaction, *Appl. Catal., B*, 2012, **125**, 59–66.
- 33 D. Voiry, *et al.*, Enhanced catalytic activity in strained chemically exfoliated WS<sub>2</sub> nanosheets for hydrogen evolution, *Nat. Mater.*, 2013, **12**(9), 850–855.
- 34 Y. Feng, *et al.*, Tailoring the properties of UiO-66 through defect engineering: A review, *Ind. Eng. Chem. Res.*, 2019, **58**(38), 17646–17659.
- 35 M. Ali, *et al.*, A review on the recent developments in zirconium and carbon-based catalysts for photoelectrochemical water-splitting, *Int. J. Hydrogen Energy*, 2021, **46**(35), 18257–18283.
- 36 H. Zhu, *et al.*, When cubic cobalt sulfide meets layered molybdenum disulfide: a core-shell system toward synergistic electrocatalytic water splitting, *Adv. Mater.*, 2015, **27**(32), 4752–4759.
- 37 J. Zhang, *et al.*, Interface engineering of MoS<sub>2</sub>/Ni<sub>3</sub>S<sub>2</sub> heterostructures for highly enhanced electrochemical overall-water-splitting activity, *Angew. Chem., Int. Ed. Engl.*, 2016, **128**(23), 6814–6819.
- 38 Z. Liu, *et al.*, Colloidal synthesis of 1T' phase dominated WS<sub>2</sub> towards durable electrocatalysis, *Nano Energy*, 2018, **50**, 176–181.
- 39 S. Liu, *et al.*, Ultrathin WS<sub>2</sub> nanosheets vertically aligned on TiO<sub>2</sub> nanobelts as efficient alkaline hydrogen evolution electrocatalyst, *Int. J. Hydrogen Energy*, 2020, **45**(3), 1697–1705.
- 40 M. Tayebi, Z. Masoumi and B.-K. Lee, Ultrasonically prepared photocatalyst of W/WS<sub>2</sub> nanoplates with WS<sub>2</sub> nanosheets as 2D material for improving photoelectrochemical water splitting, *Ultrason. Sonochem.*, 2021, **70**, 105339.
- 41 M. Velpandian, *et al.*, Improved charge carrier dynamics of WS<sub>2</sub> nanostructures by the way of CdS@WS<sub>2</sub> heterostructures for use in water splitting and water purification, *Sustainable Energy Fuels*, 2020, **4**(8), 4096–4107.
- 42 S. Peng, *et al.*, Engineering Co<sub>9</sub>S<sub>8</sub>/WS<sub>2</sub> array films as bifunctional electrocatalysts for efficient water splitting, *J. Mater. Chem. A*, 2017, **5**(44), 23361–23368.
- 43 A. Roy, P. Kalita and B. Mondal, Structural, spectroscopic and electrical properties of liquid phase exfoliated few layered two-dimensional tungsten disulfide (WS<sub>2</sub>) using anionic surfactant, *J. Mater. Sci.: Mater. Electron.*, 2023, **34**(3), 224.
- 44 D. Ovchinnikov, *et al.*, Electrical transport properties of single-layer WS<sub>2</sub>, *ACS Nano*, 2014, **8**(8), 8174–8181.
- 45 H.-L. Tsai, *et al.*, Exfoliated – restacked phase of WS<sub>2</sub>, *Chem. Mater.*, 1997, **9**(4), 879–882.
- 46 M. N. Uddin, *et al.*, Improving water-splitting efficiency of water electrolysis process via highly conductive nanomaterials at lower voltages, *Energy, Ecol. Environ.*, 2020, **5**, 108–117.
- 47 G. Yang, *et al.*, Role of electron pathway in dimensionally increasing water splitting reaction sites in liquid electrolytes, *Electrochim. Acta*, 2020, **362**, 137113.
- 48 X. Zhang, *et al.*, Preparation and tribological properties of WS<sub>2</sub> hexagonal nanoplates and nanoflowers, *Nanomaterials*, 2019, **9**(6), 840.
- 49 Z. Liu, *et al.*, Colloidal synthesis of 1T' phase dominated WS<sub>2</sub> towards durable electrocatalysis, *Nano Energy*, 2018, **50**, 176–181.
- 50 X.-F. Zhang, *et al.*, Adsorptive desulfurization from the model fuels by functionalized UiO-66 (Zr), *Fuel*, 2018, **234**, 256–262.
- 51 A. R. Bushroa, *et al.*, Approximation of crystallite size and microstrain via XRD line broadening analysis in TiSiN thin films, *Vacuum*, 2012, **86**(8), 1107–1112.
- 52 A. Schaate, *et al.*, Modulated synthesis of Zr-based metal-organic frameworks: from nano to single crystals, *Chem. - Eur. J.*, 2011, **17**(24), 6643–6651.
- 53 H. Chen, *et al.*, Silver nanoparticles on UiO-66 (Zr) metal-organic frameworks for water disinfection application, *Food Sci. Hum. Wellness*, 2022, **11**(2), 269–276.
- 54 S. Swathi, *et al.*, Surfactant-assisted tungsten sulfide mesoporous sphere for hydrogen production, *Int. J. Hydrogen Energy*, 2021, **47**(100), 41984–41993.
- 55 M. A. Ehsan, A. S. Hakeem and A. Rehman, Synergistic effects in bimetallic Pd-CoO electrocatalytic thin films for oxygen evolution reaction, *Sci. Rep.*, 2020, **10**(1), 1–11.
- 56 M. S. Amer, *et al.*, Bifunctional electrocatalyst of low-symmetry mesoporous titanium dioxide modified with cobalt oxide for oxygen evolution and reduction reactions, *Catalysts*, 2019, **9**(10), 836.
- 57 L. Yu, *et al.*, Hierarchical Cu@CoFe layered double hydroxide core-shell nanoarchitectures as bifunctional electrocatalysts for efficient overall water splitting, *Nano Energy*, 2017, **41**, 327–336.
- 58 D. Zhao, *et al.*, Bifunctional ZnCo<sub>2</sub>S<sub>4</sub>@CoZn<sub>13</sub> hybrid electrocatalysts for high efficient overall water splitting, *J. Energy Chem.*, 2022, **69**, 292–300.
- 59 W. Zhang, *et al.*, Multi-active site CoNi-MOFs as non-noble bifunctional electrocatalysts for highly efficient overall water splitting, *Int. J. Hydrogen Energy*, 2022, **47**(3), 1633–1643.
- 60 L. Zhi, *et al.*, 3D holey hierarchical nanoflowers assembled by cobalt phosphide embedded N-doped carbon nanosheets as bifunctional electrocatalyst for highly efficient overall water splitting, *J. Colloid Interface Sci.*, 2022, **616**, 379–388.
- 61 L. Zhi, *et al.*, 3D holey hierarchical nanoflowers assembled by cobalt phosphide embedded N-doped carbon nanosheets as bifunctional electrocatalyst for highly efficient overall water splitting, *J. Colloid Interface Sci.*, 2022, **616**, 379–388.
- 62 Z. Xu, *et al.*, Co(OH)<sub>2</sub> Nanoflowers Decorated  $\alpha$ -NiMoO<sub>4</sub> Nanowires as a Bifunctional Electrocatalyst for Efficient Overall Water Splitting, *Catalysts*, 2022, **12**(11), 1417.
- 63 X. Hu, *et al.*, Nickel foam and stainless steel mesh as electrocatalysts for hydrogen evolution reaction, oxygen evolution reaction and overall water splitting in alkaline media, *RSC Adv.*, 2019, **9**(54), 31563–31571.



- 64 P. Connor, *et al.*, The determination of electrochemical active surface area and specific capacity revisited for the system MnOx as an oxygen evolution catalyst, *Z. Phys. Chem.*, 2020, **234**(5), 979–994.
- 65 G. Zhang, *et al.*, Phosphorus and yttrium codoped Co (OH) F nanoarray as highly efficient and bifunctional electrocatalysts for overall water splitting, *Small*, 2019, **15**(42), 1904105.
- 66 V. Charles, *et al.*, CoOx/UiO-66 and NiO/UiO-66 heterostructures with UiO-66 frameworks for enhanced oxygen evolution reactions, *New J. Chem.*, 2021, **45**(32), 14822–14830.
- 67 P. M. Pataniya and C. Sumesh, Enhanced electrocatalytic hydrogen evolution reaction by injection of photogenerated electrons in Ag/WS<sub>2</sub> nanohybrids, *Appl. Surf. Sci.*, 2021, **563**, 150323.
- 68 X. Shi, *et al.*, Rapid flame doping of Co to WS<sub>2</sub> for efficient hydrogen evolution, *Energy Environ. Sci.*, 2018, **11**(8), 2270–2277.
- 69 L. Yang, *et al.*, Amorphous nickel/cobalt tungsten sulfide electrocatalysts for high-efficiency hydrogen evolution reaction, *Appl. Surf. Sci.*, 2015, **341**, 149–156.
- 70 Q. Yang, *et al.*, Composite electrocatalyst Mo<sub>x</sub>W<sub>1-x</sub>S<sub>2</sub> nanosheets on carbon fiber paper for highly efficient hydrogen evolution reaction, *J. Solid State Electrochem.*, 2018, **22**(10), 2969–2976.
- 71 Z. Huang, *et al.*, Polyoxometallates@zeolitic-imidazolate-framework derived bimetallic tungsten-cobalt sulfide/porous carbon nanocomposites as efficient bifunctional electrocatalysts for hydrogen and oxygen evolution, *Electrochim. Acta*, 2020, **330**, 135335.

